

# AKARI Near- to Mid-Infrared Imaging and Spectroscopic Observations of the Small Magellanic Cloud. I. Bright Point Source List

Yoshifusa ITA

<sup>1</sup>*National Astronomical Observatory of Japan, 2-21-1 Osawa, Mitaka, Tokyo, 181-8588, Japan  
yoshifusa.ita@nao.ac.jp*

Takashi ONAKA<sup>2</sup>, Toshihiko TANABÉ<sup>3</sup>, Noriyuki MATSUNAGA<sup>3</sup>, Mikako MATSUURA<sup>4</sup>,  
Issei YAMAMURA<sup>5</sup>, Yoshikazu NAKADA<sup>3</sup>, Hideyuki IZUMIURA<sup>6</sup>, Toshiya UETA<sup>7</sup>,  
Hiroyuki MITO<sup>8</sup>, Hinako FUKUSHI<sup>3</sup>, and Daisuke KATO<sup>2</sup>

<sup>2</sup>*Department of Astronomy, Graduate School of Science, The University of Tokyo, Bunkyo-ku, Tokyo 113-0033, Japan*

<sup>3</sup>*Institute of Astronomy, Graduate School of Science, The University of Tokyo, 2-21-1 Osawa, Mitaka, Tokyo 181-0015, Japan*

<sup>4</sup>*Department of Physics and Astronomy, University College London, Gower Street, London WC1E 6BT, United Kingdom*

<sup>5</sup>*Institute of Space and Astronautical Science, Japan Aerospace Exploration Agency  
3-1-1 Yoshinodai, Sagami-hara, Kanagawa 229-8510, Japan*

<sup>6</sup>*Okayama Astrophysical Observatory, National Astronomical Observatory of Japan,  
Kamogata, Asakuchi, Okayama 719-0232, Japan*

<sup>7</sup>*Department of Physics and Astronomy, University of Denver, 2112 E. Wesley Avenue, Denver, CO 80208, USA*

<sup>8</sup>*The KISO observatory, Tarusawa 10762-30, Mitake, Kiso, Nagano 397-0101, Japan*

(Received 0 0; accepted 0 0)

## Abstract

We carried out a near- to mid-infrared imaging and spectroscopic observations of the patchy areas in the Small Magellanic Cloud using the Infrared Camera on board AKARI. Two 100 arcmin<sup>2</sup> areas were imaged in 3.2, 4.1, 7, 11, 15, and 24  $\mu\text{m}$  and also spectroscopically observed in the wavelength range continuously from 2.5 to 13.4  $\mu\text{m}$ . The spectral resolving power  $\lambda/\Delta\lambda$  is about 20, 50, and 50 at 3.5, 6.6 and 10.6  $\mu\text{m}$ , respectively. Other than the two 100 arcmin<sup>2</sup> areas, some patchy areas were imaged and/or spectroscopically observed as well. In this paper, we overview the observations and present a list of near- to mid-infrared photometric results, which lists  $\sim 12,000$  near-infrared and  $\sim 1,800$  mid-infrared bright point sources detected in the observed areas. The  $10\sigma$  limits are 16.50, 16.12, 13.28, 11.26, 9.62, and 8.76 in Vega magnitudes at 3.2, 4.1, 7, 11, 15, and 24  $\mu\text{m}$  bands, respectively.

**Key words:** Galaxies:Magellanic clouds infrared:stars stars:AGB and post-AGB

## 1. Introduction

The Small Magellanic Cloud (SMC) is among the nearest neighbor galaxies of the Milky Way, along with its companion, the Large Magellanic Cloud (LMC). It is well known that some physical properties of the SMC are different from those of the Milky Way: Its mean metallicity is lower ( $\sim 1/10$ ) than that of the solar vicinity (e.g., Dufour et al. 1982; Dufour et al. 1984; Westerlund 1997 and references therein), its average dust to gas mass ratio is significantly lower than that in the Milky Way (The actual value remains largely uncertain, ranging from  $\sim 1/5$  (Gordon et al. 2003) to  $1/30$  (Stanimirovic et al. 2000) of the Galactic value), and its interstellar UV radiation field is stronger than that in the Milky Way (Dickey et al. 2000). Therefore, we can study environmental effects on various aspects of astrophysical processes if we observe celestial objects in the Large and Small Magellanic Clouds (MCs) and Milky Way, and compare the results.

The MCs have been extensively surveyed by various types of instruments at a wide variety of wavelengths

(from X-ray to Radio). Especially, in terms of mid-infrared observational data of the MCs, there are drastic advancements recently. Bolatto et al. (2006) observed the main part of the SMC with the *Spitzer* Space Telescope (SST), and provided a photometric catalog of  $\sim 4\times 10^5$  near- to far-infrared point sources. A more extensive survey toward the SMC using the SST was then carried out by Gordon et al. (2010), and they delivered a comprehensive point source catalog that lists  $\sim 1.2\times 10^6$  sources. Meanwhile, Meixner et al. (2006) and Ita et al. (2008) observed a large part of the LMC in near- to far-infrared wavebands using the SST and AKARI satellite, respectively. These results are significant leaps from the IRAS (Israel & Schwering 1986) and MSX (Egan et al. 2003) data, regarding to sensitivity and spatial resolving power.

We made imaging and spectroscopic observations of the central part of the SMC using the Infrared Camera (IRC; Onaka et al. 2007) on board AKARI (Murakami et al. 2007). This is a part of the AKARI Open Time Program, “The role of pulsation in mass loss along the Asymptotic Giant Branch (PI. Y.Ita)”. This program was arranged to

obtain photometric data of the complete spectral energy distribution from near- to mid-infrared wavelengths, and also spectra in the same wavelength range for a statistically significant number of variable stars of various types. Ita et al. (2002, 2004a) are conducting a near-infrared ( $J$ ,  $H$ , and  $K_s$ ) monitoring survey in the MCs since 2000. See the references for the outline of the monitoring survey and its initial results. This monitoring observation showed that significant fractions of red giants are variable stars of a wide variety of types pulsating in diverse pulsation modes. A primary goal of the program is to study how the mass loss depends on the overall characteristics of a variable star, for instance its time-averaged absolute luminosity or its mass, its pulsation period, amplitude, dominant pulsation mode, and its surface chemistry.

In this paper we outline our AKARI IRC observations in the SMC, and present near- to mid-infrared point source lists. We concentrate on the imaging data and make general analyses using the point source lists. We study infrared color-magnitude diagrams and spectral energy distributions to identify several types of interesting objects. This paper is a companion piece to the work of AKARI IRC imaging/spectroscopic survey of the LMC (PI. T. Onaka; see Ita et al. 2008 for survey descriptions), and the results obtained here can be directly compared with the ones obtained in the LMC survey. Analyses and discussions on the spectroscopic data will be made in a separate paper. Also, the relevance between pulsation characteristics and mass loss from red giants will be described elsewhere and is not discussed in this paper.

## 2. Observations

We obtained near- to mid-infrared imaging and spectroscopic data for selected areas in the SMC using the IRC on board AKARI. The observed areas are shown in Figure 1, and their central coordinates are listed in Table 1. These areas are selected based on the results from our near-infrared monitoring survey to ensure that they contain various types of variable red giants of different mass-loss rates.

As is described in the IRC data user’s manual (Lorente et al. 2007), the IRC is comprised of three independent channels; NIR, MIRS, and MIRL, which cover the  $1.8 - 5.5 \mu\text{m}$ ,  $4.6 - 13.4 \mu\text{m}$ , and  $12.6 - 26.5 \mu\text{m}$  wavelength range, respectively. Each of the channels has a field of view of about  $10' \times 10'$ . There are several types of observing templates for the observations with the IRC. Among them, we used the IRC AOT02 observing template with the nominal option. With the configuration, an pointed observation will yield imaging data at  $3.2$  (N3),  $4.1$  (N4),  $7.0$  (S7),  $11.0$  (S11),  $15.0$  (L15), and  $24.0 \mu\text{m}$  (L24, the acronyms standing for the IRC bands are in the parentheses, and will be used hereafter) of at least three dithered sky positions, suitable to cover a wide range of the spectral energy distribution (SED) of a celestial body. We have to note that due to the layout of the IRC’s three channels, the center of the MIRL (L15 and L24) channel is slightly ( $\sim 15'$ ) offset from that of the NIR (N3

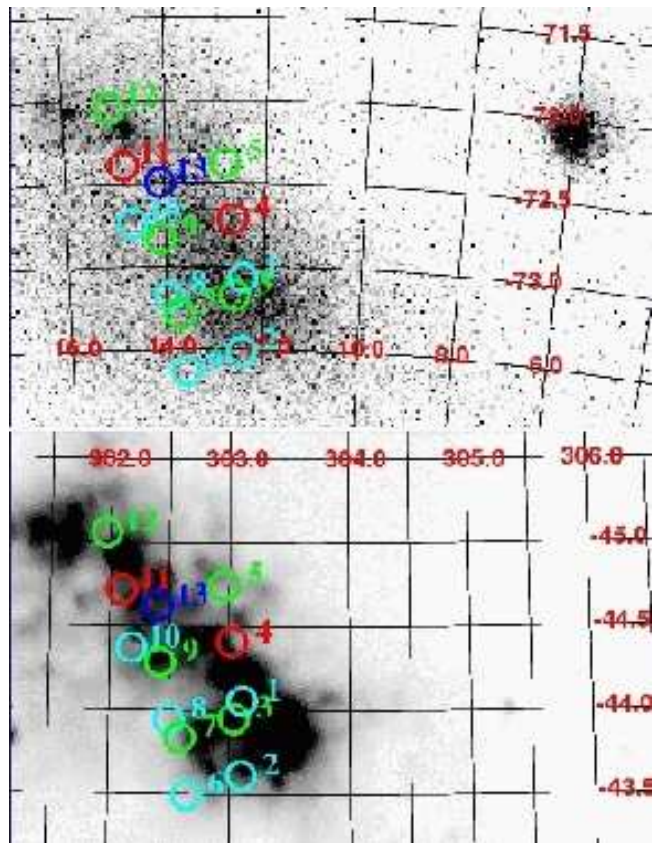


**Fig. 1.** A graphic representation of the AKARI IRC observations in the SMC. The background images are optical DSS image (upper panel) and IRAS  $100 \mu\text{m}$  image (lower panel). North is up, and east is to the left. The coordinate grids are in degrees on equatorial J2000 system (upper panel) and galactic (lower panel). The circles and their associated numbers indicate the positions and ID numbers of the observed areas listed in Table 1. The diameter of the circles is  $10'$ , which is identical to the field of views of IRC’s arrays. Red circles show that both of the NIR/MIRS and MIRL imaging data are obtained for the corresponding areas. Cyan (green) circles mean only NIR/MIRS (MIRL) data are available, and blue circles indicate only spectroscopic data are available for the corresponding positions, respectively.

and N4) and MIRS (S7 and S11) channels. Therefore, two pointed observations are necessary to obtain a complete imaging dataset (i.e., to get imaging data in all IRC bands mentioned above) for a  $10' \times 10'$  area. IRC observations produce short- and long-exposure data together. The long to short exposure time ratios in each channel are 9.5, 28, and 28 for NIR, MIRS, and MIRL, respectively. We can enhance the dynamic range by combining photometric results of the two different exposure-time data. In this paper, we use both long- and short-exposure data as described in the next section.

In addition, for some of the areas, we used IRC AOT04 observing template to obtain near- to mid-infrared (continuously from  $2.5$  to  $13.4 \mu\text{m}$ ) low-resolution spectra for all bright sources present in the field of views. The spectral resolving powers ( $\lambda/\Delta\lambda$ ) are about 20, 50, and 50 at  $3.5$ ,  $6.6$ , and  $10.6 \mu\text{m}$ , respectively (Ohya et al. 2007).

We will describe the spectroscopic observations in a separate paper.

The observations were planned to be carried out in two separate seasons, one from late April to early May of 2007, and the other in early November of 2007. The latter part of the observations was canceled because AKARI ran out of its on-board supply of cryogen, liquid Helium on August 26, 2007. As a result, eight and five pointed observations were carried out for imaging and spectroscopic observations, respectively. Unfortunately, an imaging observation data was lost because of the downlink problem. The remaining pointed observational data yield a complete dataset (i.e., imaging data in 3.2 to 24  $\mu\text{m}$  and also spectroscopic data from 2.5 to 13.4  $\mu\text{m}$ ) for two 100 arcmin<sup>2</sup> areas and incomplete dataset (with NIR&MIRS but without MIRL, or vice versa) for five 100 arcmin<sup>2</sup> areas. Table 1 summarizes the datasets available for each observed position.

**Table 1.** Central positions of the observed areas in the SMC. Each area is about  $10' \times 10'$  wide. The "o/x" indicates that photometric or spectroscopic data for the corresponding area is "available/unavailable".

ID	Central position		Imaging		Sp <sup>1</sup>
	R.A.	Dec.	N3,4	L15	
	degrees, J2000		S7,11	L24	
1	12.429260	-73.069321	o	x	x
2	12.434312	-73.514125	o	x	o
3	12.592758	-73.174783	x	o	x
4	12.641994	-72.716711	o	o	o
5	12.808702	-72.380207	x	o	x
6	13.587801	-73.630897	o	x	x
7	13.718320	-73.287865	x	o	x
8	13.936132	-73.179619	o	x	x
9	14.099293	-72.835420	x	o	o
10	14.668618	-72.743250	o	x	x
11	14.825172	-72.395937	o	o	o
12	15.070746	-72.050904	x	o	x
13	14.111987	-72.496630	x	x	o

<sup>1</sup> Spectroscopic observation (from 2.5 to 13.4  $\mu\text{m}$ )

### 3. Data reduction and compilation of the point source list

#### 3.1. Photometry

Raw imaging data are processed with the IRC imaging toolkit, version 20071017 (see IRC Data User's Manual Lorente et al. 2007 for details). Remember that the adopted AKARI IRC observing templates produces at least three images taken at different sky positions for each filter. The toolkit aligns the images and combine them to make a stacked image. We perform photometry on the stacked images using IRAF<sup>1</sup>/DAOPHOT package.

<sup>1</sup> IRAF is distributed by the National Optical Astronomy Observatories, which are operated by the Association of

We develop point spread function (PSF) fitting photometry software, which is similar to the one that the *Spitzer* GLIMPSE<sup>2</sup> (Benjamin et al. 2003) team uses. Our photometric process involves the following steps:

1. DAOFIND is used to extract point-like sources whose fluxes are more than  $2\sigma$  above the background.
2. Aperture photometry is performed on the extracted sources by using the aperture radius of 10 pixels for N3 and N4 images, and of 7.5 pixels for others. These radii are the same ones that are used to do absolute photometric calibrations with standard stars (see Tanabé et al. 2008). Therefore, we do not need to apply aperture corrections. The inner radii of the sky annulus are the same as the aperture radii. We chose the width of the sky annulus to be 10 pixels.
3. The resultant instrumental fluxes are converted into the physical units by using the IRC flux calibration constants version 20071112. Then the calibrated fluxes are converted into magnitudes on the IRC-Vega system by using the zero magnitude fluxes listed in Tanabé et al. (2008). The differences between the instrumental and the calibrated magnitudes are constants.
4. Photometry processes for the S7, S11, L15 and L24 short exposure images stop here.
5. Several isolated (without other sources within 7 pixels) point sources with moderate flux (i.e., with a good signal-to-noise ratio and unsaturated) are selected from the results of step 2. At least 8 such "good" stars are selected in the N3, N4, S7, and S11 images, and more than 5 good stars in the L15 and L24 images. These good stars are used when applying the aperture corrections to the PSF fitting photometry results described in the following process.
6. Since the shapes of the PSFs measurably vary from pointing to pointing in the N3 and N4 images possibly due to jitters in the satellite pointing, the selected good stars in step 5 are used to construct a model PSF for each image. We use DAOPHOT to choose the best fitting function by trying several different types of fitting functions. In the S7, S11, L15 and L24 images, we use grand-PSFs for each band that were built in advance using data from the LMC survey (Ita et al. 2008) and the 47 Tuc observation (Ita et al. 2007). These grand-PSFs were made from "good" stars free from diffuse emission, carefully chosen by eyes.
7. The PSF fitting photometry is performed on the extracted sources in step 1 using ALLSTAR. We let the PSF vary linearly over the image. This PSF fitting operation is iterated three times, in just the same way as the GLIMPSE team does.

Universities for Research in Astronomy, Inc., under cooperative agreement with the National Science Foundation.

<sup>2</sup> Visit <http://www.astro.wisc.edu/glimpse/>, and see a document "Description of Point Source Photometry Steps Used by GLIMPSE", written by Dr. Brian L. Babler.

8. Aperture correction is applied to the fit magnitudes by comparing them with the aperture magnitudes of good stars, which are selected in step 5. Then, the offset value obtained in step 3 is added to the aperture corrected fit magnitudes to derive calibrated fit magnitudes.

We have to note that photometric errors calculated by the IRAF/DAOPHOT ignore contributions from read-out noises, that are non-negligible in IRC's NIR bands. Therefore we add read-out noises to the photometric uncertainties.

Those who want to convert magnitudes into Janskies, refer to Tanabé et al. (2008), and the zero-magnitude fluxes for each band are tabulated in Table 3. It should be noted that the IRC absolute flux calibration assumes a spectral energy distribution (SED) of  $f_\lambda \propto \lambda^{-1}$  or  $f_\nu \propto \nu^{-1}$ . One should apply color-corrections depending on the source spectrum.

### 3.2. Astrometry

For each of the long exposure images, we calculate the coordinate transform matrix that relates the image pixel coordinates to the sky coordinates by matching the detected point sources with the Two Micron All Sky Survey (2MASS; Skrutskie et al. 2006) catalog. We use at least five matched point sources for the calculation. Then, we use the same matrix to the corresponding short exposure image. The root-mean-squares of the residuals between the input catalog coordinates and the fitted coordinates are found to be smaller than  $0''.8$ ,  $0''.8$ , and  $1''.4$ , for NIR, MIRS, and MIRL images, respectively<sup>3</sup>. The coordinates of the AKARI sources should be accurate to that extent relative to the 2MASS coordinates.

### 3.3. Point source list and its explanation

The above analysis produces four photometric results for an observed area for the N3 and N4 images, corresponding the differences in the photometry method (aperture/fit) and in the exposure time (short/long). Meanwhile, there are three photometric results for an observed area for the S7, S11, L15 and L24 images, because we did not perform fit photometry to their short exposure data. Among these photometric results, we only use results from fit photometry for the N3 and N4 images. For the S7, S11, L15 and L24 images, we use results from fit photometry for long exposure images, but from aperture photometry for short ones.

To enhance the dynamic range, we merge the photometric results from short and long exposure data using positional tolerances of  $3''.0$  for N3, N4, S7 and S11 images, and  $5''.0$  for L15 and L24 images. If a source is detected in both short and long exposure data, we adopt the one with a better S/N and discard the other. The adopted photometry method and exposure time are indicated by flags in the point source list (see below).

Similar to the *Spitzer* IRAC (Fazio et al. 2004a) images, the N3 and N4 images suffer from the mux bleed (flux leaks from bright point sources, making false faint point-like sources every 4th pixels along a row in which the bright sources are found) and column pulldown (reduction in intensity of the columns in which bright sources are found) effect. We did not try to correct these effects. Instead, we just identify and flag out the suspected victims that are located within belts of  $\pm 5$ -pixels wide along the rows/columns where the bright (saturated) sources are found. These effects are not seen in the S7, S11, L15 and L24 images. We also flag out sources that are located near the bright sources, using the proximity radius of 20 pixels for N3 and N4, and of 15 pixels for the others. Furthermore, the S7 and S11 images suffer from notable ghost images of bright sources due to the internal reflections in the beam splitter (Lorente et al. 2007). The positions of ghosts, which depend on the real source positions, are well determined, and we also flag out the suspected ghosts. Faint ghosts are present, but not significant in the N3, N4, L15 and L24 images.

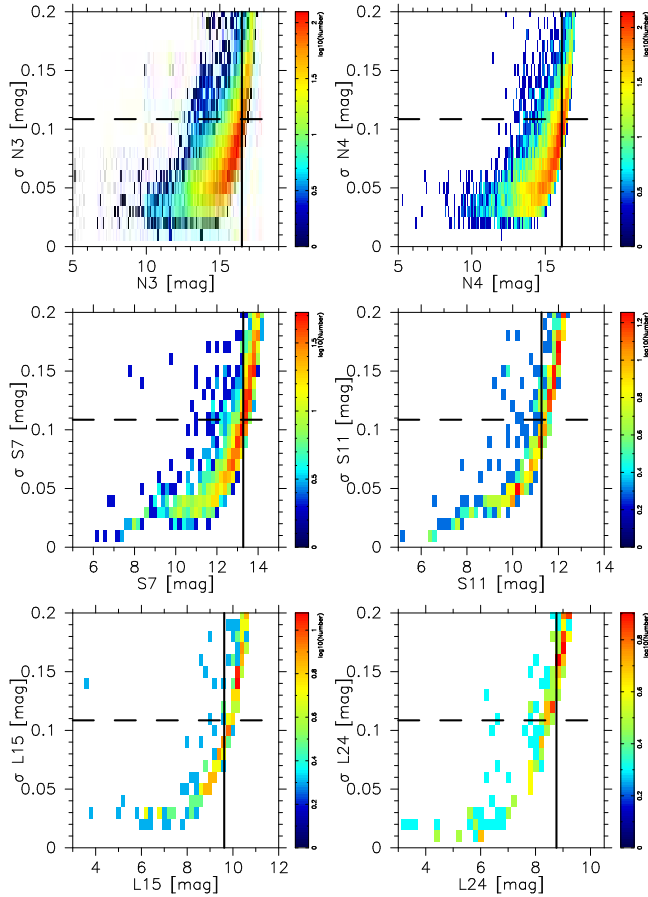
Finally, we eliminate possible false detections in the following way. Very recently, *Spitzer* SAGE-SMC survey (PI. K. Gordon) delivered the photometry catalog (SAGE-SMC catalog; Gordon et al. 2010). Although the band-passes of the AKARI IRC and the *Spitzer* IRAC/MIPS bands are different, a source detected in an IRC band is likely to be detected in the closely matched *Spitzer* band. Based on the idea, we match N3 with [3.6], N4 with [4.5], S7 with [8.0], S11 with [8.0], L15 with [8.0], and L24 with [24] with a positional tolerance of  $3''.0$ . The numbers bracketed by [ ] designates the data of the SAGE-SMC catalog, for example, [3.6] indicates the data of the IRAC 3.6  $\mu\text{m}$  band. There are two types of the SAGE-SMC catalog. One is the "Catalog", which is a more highly reliable list. The other is the "Archive/Full", which is a more complete list. See the explanatory document "The SAGE-SMC Data Description" prepared by K. Gordon for more detailed descriptions. We only list sources that have counterparts in the SAGE-SMC Archive/Full catalog. The eliminated sources are likely to be false detections around bright stars and mux bleeds for N3 and N4, and due to false detections in nebulous fields for the S7, S11, L15, and L24.

Table 2 shows the first five records of the point source list for the N3 data as an example. The full version of the list, and lists for other IRC bands are available at <http://www.somewhere.in.a.website/>. The first two columns show the AKARI coordinates on the J2000 system. The following two columns show photometric results and their uncertainties in Vega magnitudes. *The magnitudes on the list are not corrected for the interstellar extinction.* The photometric uncertainty includes errors in the magnitude calculated by IRAF corrected for the contributions from read-out noise, in the aperture correction factor, and also in the ADU-to-Jy conversion factor. The next column shows the observing date in UT. The following six columns show the various flags; S0L1 denotes photometry comes either from short (0) or long (1)

<sup>3</sup> The pixel field of views of each IRC channel are tabulated in the table 3.

data, A0F1 denotes the photometry method, 0 for aperture photometry and 1 for fit photometry, SAT is set to 1 if a bright source is in proximity, COL and MUX are set to 1 if the star is located in the mux-bleed and column pulldown belt, and GHO is set to 1 if the star is suspected to be a ghost. The next four columns show positions and magnitudes of the source found in the closely matched band in the SAGE-SMC Archive/Full catalog.

**Table 2.** The first five records of the AKARI/IRC bright point source list in the SMC for N3 band. The full version of the list, and list for other IRC bands are available from <http://www.somewhere.in.a.website/>.



**Fig. 2.** Photometric uncertainties as a function of the magnitude at each IRC band. The sizes of the bins are  $0.1 \times 0.01$  mag for N3 and N4, and  $0.2 \times 0.01$  mag for S7, S11, L15, and L24. The dashed lines show  $10 \sigma$  errors, and the solid lines indicates the  $10 \sigma$  limits: 16.50, 16.12, 13.28, 11.26, 9.62, and 8.76 mag in N3, N4, S7, S11, L15, and L24, respectively.

### 3.4. $10 \sigma$ detection limits and completeness

The distributions of the photometric uncertainty versus magnitude in each IRC band are shown in Figure 2. The horizontal dashed lines show the signal to noise ratio (S/N) of 10, and the vertical solid lines show the  $10 \sigma$  limits, which are defined as the faintest magnitudes at which the  $3 \sigma$  clipped mean photometric uncertainties of sources in  $0.02$  mag bins exceed  $0.109$  mag. The estimated  $10 \sigma$  limits are 16.50, 16.12, 13.28, 11.26, 9.62, and 8.76 mag in N3, N4, S7, S11, L15, and L24, respectively.

The magnitude distributions of sources in our point source lists are shown in Figure 3. The sizes of the bins

R.A.	Dec	N3	eN3	Obsdate	S0L1	A0F1	SAT	COL	MUX	GHO	R.A.	DEC	[3.6]	e[3.6]
[degree]	(J2000)	[Vega mag]	[Vega mag]	YYYY-MM-DDTHH:MM:SS			flags				[degree]	J2000	[Vega mag]	[Vega mag]
.067157	-73.084494	13.126	0.102	2007-05-01T11:31:17	1	1	0	0	1	0	12.068133	-73.084318	13.313	0.062
.068123	-73.535214	16.816	0.204	2007-04-30T04:03:26	1	1	0	0	1	0	12.068123	-73.535266	17.286	0.129
.069061	-73.545911	15.450	0.095	2007-04-30T04:03:26	1	1	0	1	0	0	12.070043	-73.545841	15.491	0.064
.069244	-73.541954	15.328	0.074	2007-04-30T04:03:26	1	1	0	0	0	0	12.069702	-73.541938	15.234	0.086
.073468	-73.543558	16.030	0.202	2007-04-30T04:03:26	1	1	0	1	0	0	12.074690	-73.543499	15.845	0.066

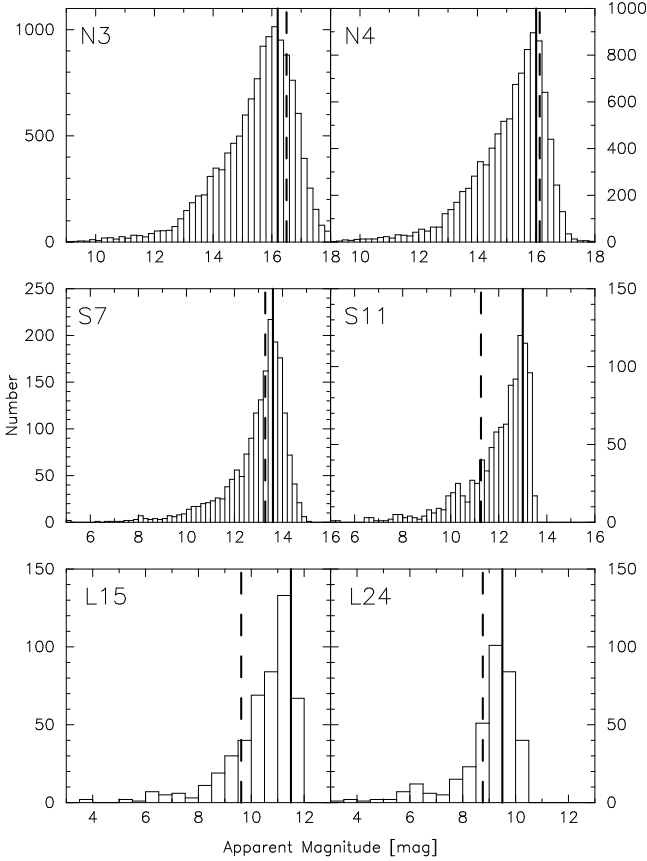


**Fig. 3.** Magnitude distribution of the sources in the AKARI/IRC SMC point source list. The sizes of the bins are 0.2 mag for N3, N4, S7, S11, and 0.5 mag for L15, and L24. The solid lines show the peak of the source count histograms, below which the photometry is incomplete: 16.2, 16.0, 13.6, 13.0, 11.5, and 9.5 mag in N3, N4, S7, S11, L15, and L24, respectively.

are 0.1 mag for N3 and N4, 0.2 mag for S7, S11, and 0.5 mag for L15 and L24, respectively. The vertical solid lines show the peak magnitudes, below which photometry is incomplete (only as a rough guide). The peak magnitudes are 16.2, 16.0, 13.6, 13.0, 11.5, and 9.5 mag in N3, N4, S7, S11, L15, and L24, respectively. The  $10\sigma$  limits for point sources and source counts in each IRC band are summarized in Table 3 together with the properties of the imaging observations.

#### 4. General analysis using the photometric list

##### 4.1. Cross-identification with the existing catalogs

We cross-identified our point source lists with the following survey catalogs using a positional tolerance of  $3''0$ , and use the results for discussion in the rest of this paper.

- The Magellanic Clouds Photometric Survey catalog (Zaritsky et al. 2002): It lists  $U, B, V,$  and  $I$  stellar photometry for the central  $18 \text{ deg}^2$  area of the SMC.
- The IRSF Magellanic Clouds Point Source Catalog (IRSF catalog; Kato et al. 2007): The IRSF catalog lists  $J, H,$  and  $K_s$  photometry of over  $2.6 \times 10^6$

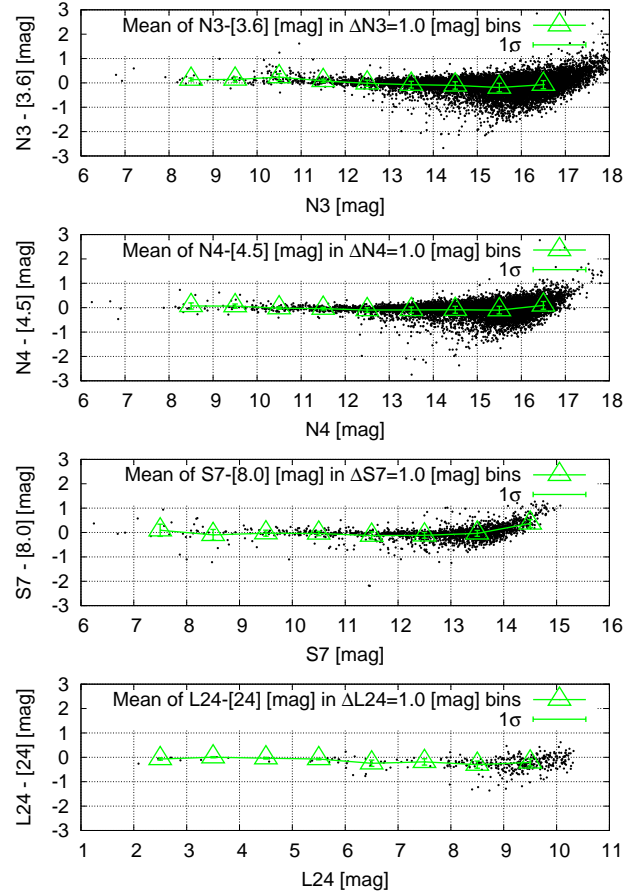


**Fig. 4.** Comparison between AKARI SMC survey and *Spitzer* SAGE-SMC survey catalog (Gordon et al. 2010) using closely matched passbands.

sources in the central  $11 \text{ deg}^2$  area of the SMC. Compared to the contemporary DENIS (Cioni et al. 2000) and 2MASS (Skrutskie et al. 2006) catalogs, the IRSF catalog is more than two mag deeper at  $K_s$  band and about four times finer in spatial resolution.

- The *Spitzer* SAGE-SMC survey catalog (Gordon et al. 2010): It lists near- to far-infrared photometry of  $\sim 1.2 \times 10^6$  sources in the SMC. Throughout this paper, the numbers bracketed by [ ] designates the data of the *Spitzer* catalog, for example, [3.6] indicates the photometry in the  $3.6 \mu\text{m}$  band.
- SMC carbon star catalog (Rebeiro, Azzopardi, & Westerlund 1993): It lists 1707 carbon stars, which are identified based on optical grism spectroscopy. Stars that classified as “Doubtful C star” and “spectrophotometry not possible” in the catalog are excluded.

We converted the IRSF system magnitudes into the 2MASS system ones by using the conversion equations given in Kato et al. (2007) and Kućinskas et al. (2008). We preferentially used equations in Kato et al. (2007), but also used ones in Kućinskas et al. (2008) when necessary.

**Table 3.** Imaging observation properties

Properties	N3	N4	S7	S11	L15	L24
Channel	NIR		MIRS		MIRL	
Pixel field of view ["/pixel]	1.446		2.340		2.384	
Bandpass [ $\mu\text{m}$ ]	2.7 - 3.8	3.7 - 5.5	5.9 - 8.4	8.5 - 13.1	12.6 - 19.4	20.3 - 26.5
Quoted wavelength [ $\mu\text{m}$ ]	3.2	4.1	7.0	11.0	15.0	24.0
10 $\sigma$ limit <sup>1</sup> [mag]	16.50	16.12	13.28	11.26	9.62	8.76
Number of sources listed	12,899	9,748	1,838	1,045	479	356
Zero magnitude flux <sup>2</sup> [Jy]	343.34	184.73	74.956	38.258	16.034	8.0459

<sup>1</sup> For point sources.

<sup>2</sup> Taken from Tanabé et al. (2008).

Because the IRSF survey did not detect bright sources (the saturation limit of the survey is about 10 mag at  $K_s$  band), we use 2MASS magnitudes for bright sources without IRSF measurements. Then, we photometrically select dusty red giants candidates with the following conditions: Sources with  $(J - K_s) > 2.0$  and  $K_s < 14$  mag. We use the term "dusty red giants" here, but a significant fraction of the sources that match these conditions can be dusty carbon stars (see Nikolaev & Weinberg 2000 for example), which are elusive in the optical spectroscopic survey.

Throughout this paper, the optical ( $U, B, V$ , and  $I$ ) and near-infrared ( $J, H$ , and  $K_s$ ) photometries are corrected for the interstellar extinction based on the relations in Cardelli, Clayton, & Mathis (1989), assuming  $A_V/E(B - V) = 3.2$ . We adopted  $(A_U, A_B, A_V, A_I, A_J, A_H, A_{K_s}) = (0.416, 0.353, 0.278, 0.163, 0.080, 0.050, 0.033)$  mag, corresponding to the total mean reddening of  $E(B - V) = 0.087$  mag derived by Udalski et al. (1999) for the OGLE's observing fields in the SMC. Any other longer wavelength photometries are not corrected for interstellar extinctions, which we assume negligible.

#### 4.2. Comparison to the SAGE-SMC catalog

Although the band profiles of the AKARI IRC and the *Spitzer* IRAC/MIPS (Fazio et al. 2004a, Rieke et al. 2004) bands are different, a comparison of closely matched bands is useful to test the calibration of the AKARI IRC data. We compared the IRC N3, N4, S7, and L24 photometries in our point source list with the corresponding 3.6, 4.5, 8.0, and 24  $\mu\text{m}$  fluxes of the sources in the SAGE-SMC catalog. Note that both of the IRC and IRAC absolute flux calibration assume a SED of  $f_\nu \propto \nu^{-1}$ , but MIPS flux scale assumes a source spectrum of a 10,000 K blackbody (MIPS Data Handbook 2007). Therefore we converted MIPS scale into IRC/IRAC one by adding  $-0.043$  mag (Bolatto et al. 2006) to the MIPS 24  $\mu\text{m}$  catalog magnitudes to make direct comparison between the L24 and MIPS 24  $\mu\text{m}$  photometries. The distributions of the magnitude differences between the IRC and IRAC/MIPS bands as a function of the corresponding IRC magnitudes are shown in Figure 4. The triangles show the mean of the residual magnitudes in the corresponding 1 mag bins, and the error bars show their standard deviation ( $1\sigma$ ). Taking account of the differences in the bandpass, the photometric results in SAGE-SMC catalog and our point source list

appear consistent with each other. Quantitatively, they are in agreement within 13, 6, 6, and 10 % in N3 vs [3.6], N4 vs [4.5], S7 vs [8.0], and L24 vs [24] for S/N > 10 sources, respectively.

#### 4.3. Color-magnitude diagrams

An advantage to study sources in the SMC is that we can make color-magnitude diagrams (CMD) of its constituent stars and can estimate their absolute magnitudes simply by subtracting a certain constant (i.e., distance modulus). Recently, Subramaniam & Subramaniam (2008) used red clump stars to estimate the line of sight depth of the Magellanic Clouds. They estimated the depth of the central part of the SMC to be as large as about 9 kpc, which corresponds to about 0.3 mag in distance modulus. In this paper, we ignore the line of sight depth of the SMC, and assume a constant distance modulus of 18.95 mag to all sources.

Preceding work by Bolatto et al. (2006) used *Spitzer* data to present infrared color-magnitude diagrams of SMC sources. Here we add S11 and L15 data, which are unique to the AKARI IRC. We use intriguing combinations of the IRC, IRAC&MIPS and IRFS/SIRIUS bands to make CMDs and the results are shown in Figure 5. The vertical axes are in apparent magnitudes. They can be scaled to the absolute magnitudes by subtracting the distance modulus. The adopted wavebands for the vertical axes are indicated at the top of each panel. The employed colors for the horizontal axes are indicated at the bottom of each panel. Spectroscopically confirmed carbon stars by optical survey (green dots), and photometrically selected dusty red giant candidates (red dots, see section 4.1 for selection criteria) are indicated.

There are really not much differences between the infrared color-magnitude diagrams in the SMC and the LMC (See figure 10 in Ita et al. 2008), in a sense that red giants, candidate of massive young stellar objects, post-AGBs and background galaxies are the dominant sources present in the diagram.

#### 4.4. Red objects

To find interesting red objects, we selected sources that are detected in  $H$ , and also in at least two wave bands among S11, L15, L24, and [24]. Then we further selected sources that satisfy at least one of the following

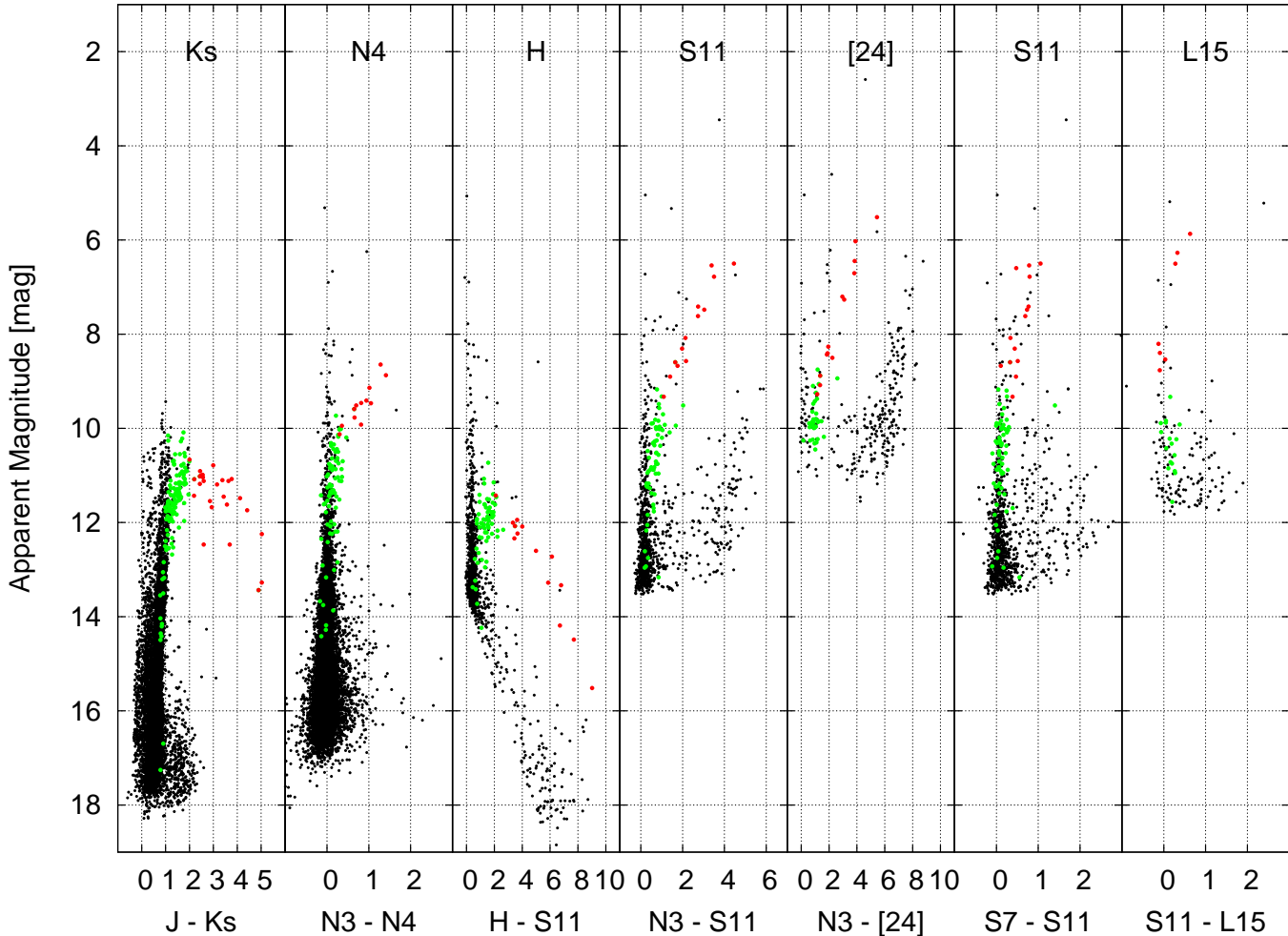


**Fig. 5.** Color magnitude diagrams of AKARI SMC sources using several combinations of IRC, IRAC, MIPS, and IRSF/SIRIUS bands. The vertical axis is in apparent magnitude at the corresponding wavebands, which are indicated at the top of each panel. Spectroscopically confirmed carbon stars (green dots) by the optical survey, and candidates of dusty red giants (red dots) are identified.

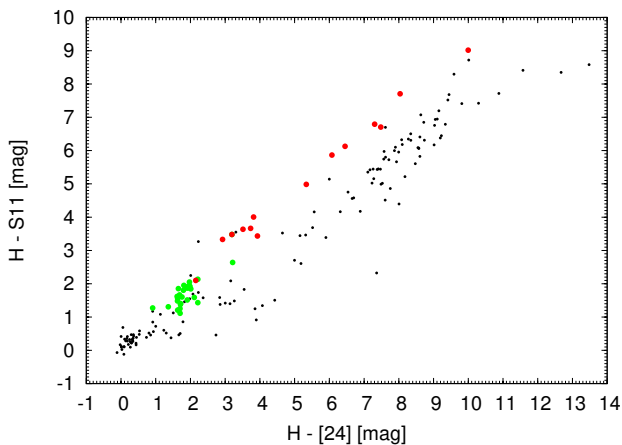


**Fig. 6.**  $H - [24]$  v.s.  $H - S11$  color-color diagram of AKARI SMC sources. Colors of the marks are as in Figure 5.

color criteria; (1)  $H - S11 > 3.0$ , (2)  $H - L15 > 3.0$ , (3)  $H - L24 > 3.0$ , (4)  $H - [24] > 3.0$ . See Figure 6 to get a rough idea of the criteria. There are 204 sources that satisfy the above criteria. We show spectral energy distributions (SED) of all the 204 sources in figure 7. Their fluxes are not color-corrected, due to the lack of information of their incident spectra. Error bars corresponding to  $\pm 1 \sigma$  in flux densities are shown, and they are usually smaller than the size of the marks. The R.A and Dec. (J2000) coordinates included in the figure are from our point source list. The solid lines show the SEDs of stars of MK spectral classes with O9V, B5V, A0V, K0III, and M0III. The relevant data were taken from Cox (2000), and we extrapolated the flux densities longward of the  $L$  band ( $\sim 3.5 \mu\text{m}$ ) by assuming Rayleigh-Jeans law. Hereafter, we call the AKARI sources by their coordinates, such as SMC12.088339–73.090576.

Then we queried the SIMBAD database with a search radius of  $3''$  for their identifications. The results are sum-



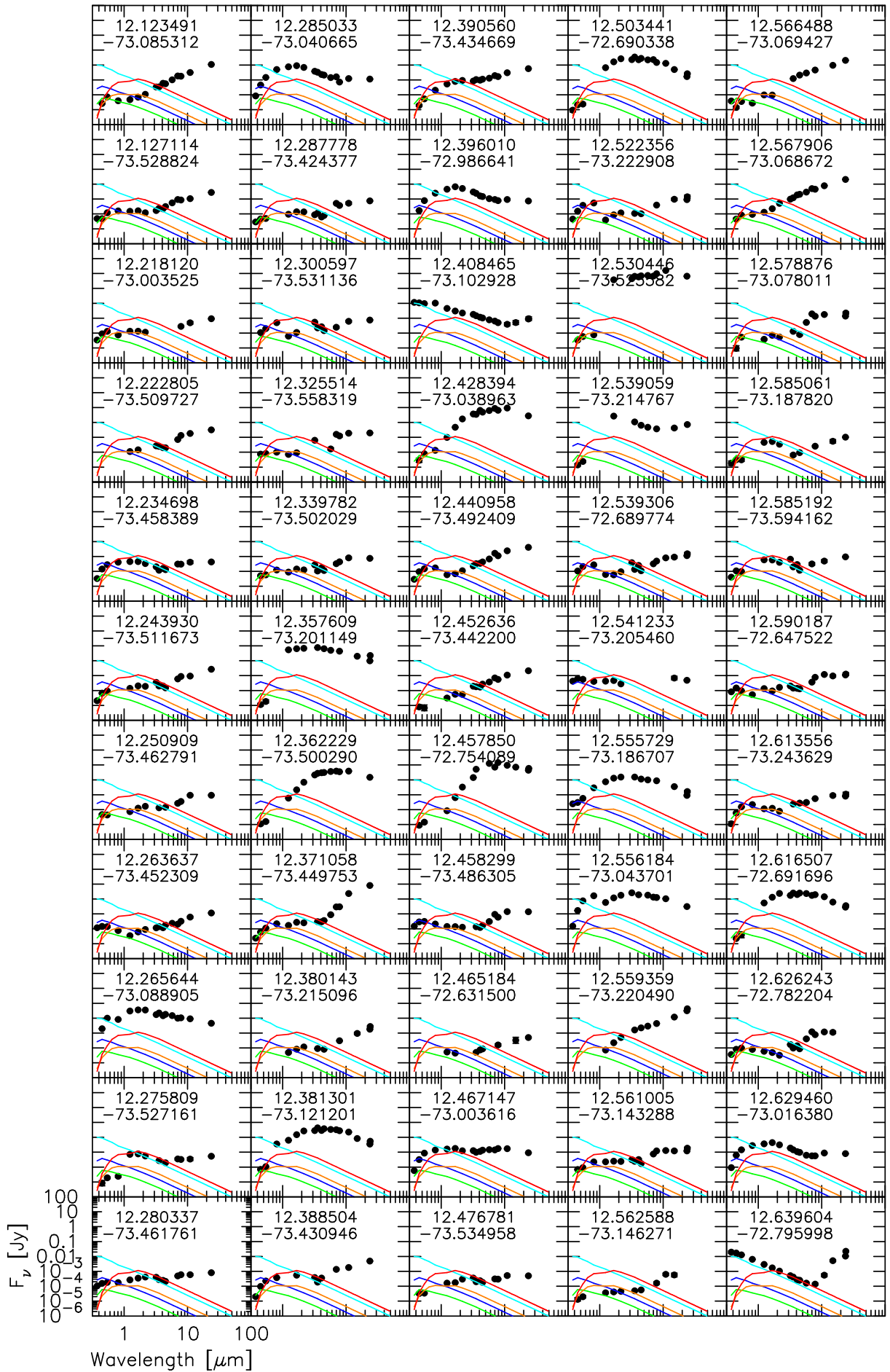


Fig. 7. The spectral energy distributions of very red AKARI/IRC sources. Note that the vertical axis is in flux densities.

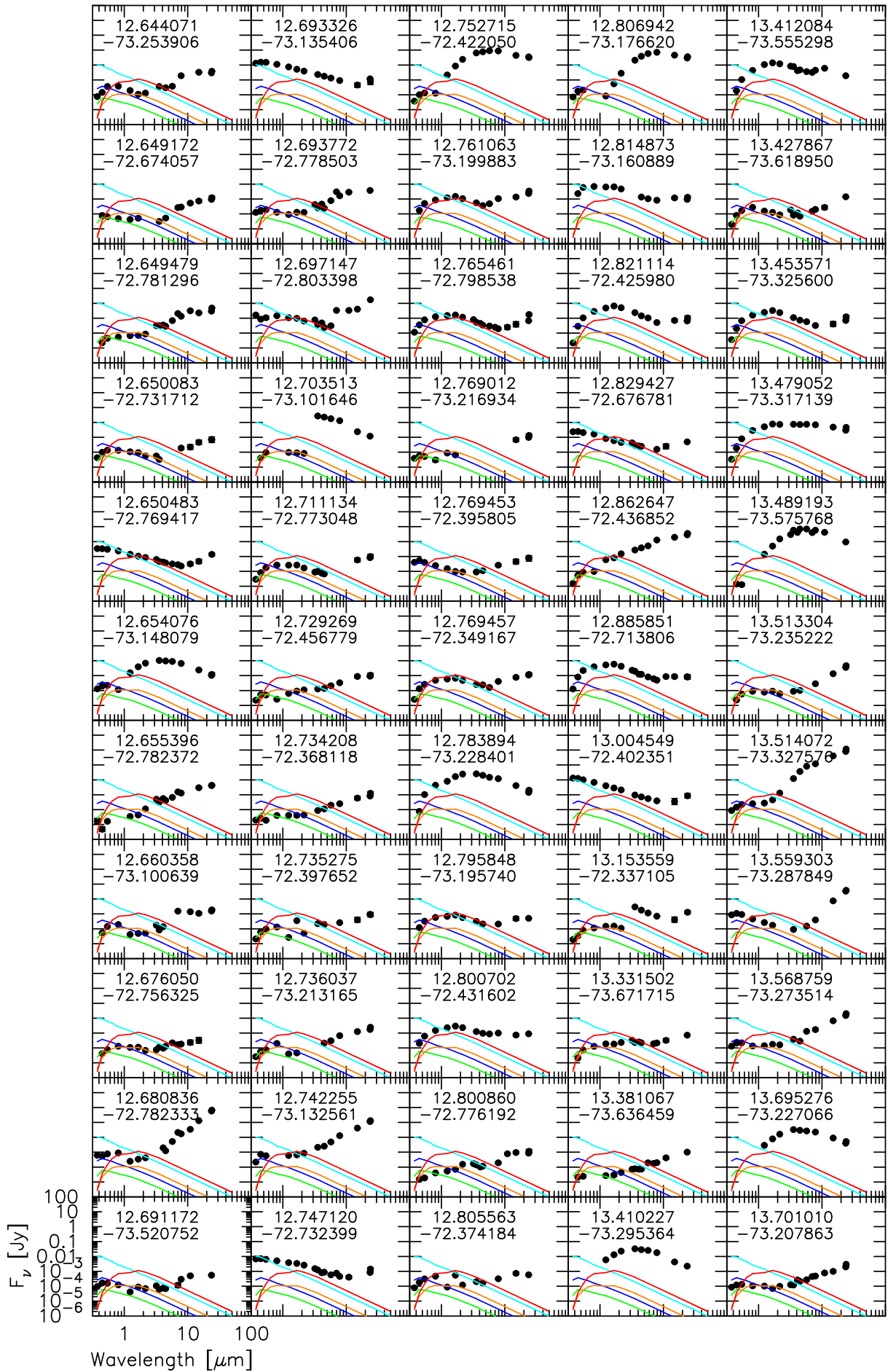


Fig. 7. The spectral energy distributions of very red AKARI/IRC sources. Note that the vertical axis is in flux densities.

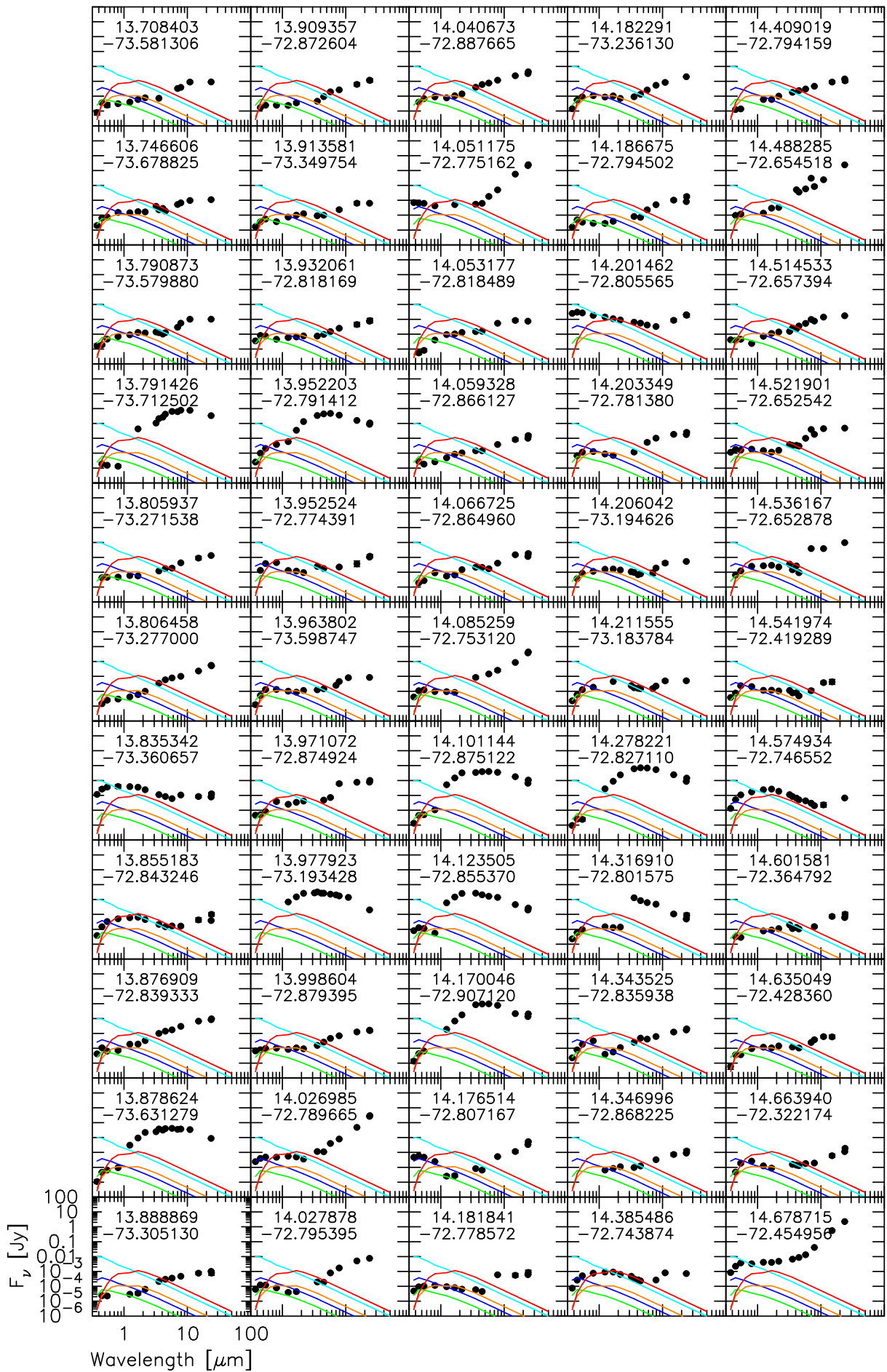


Fig. 7. The spectral energy distributions of very red AKARI/IRC sources. Note that the vertical axis is in flux densities.

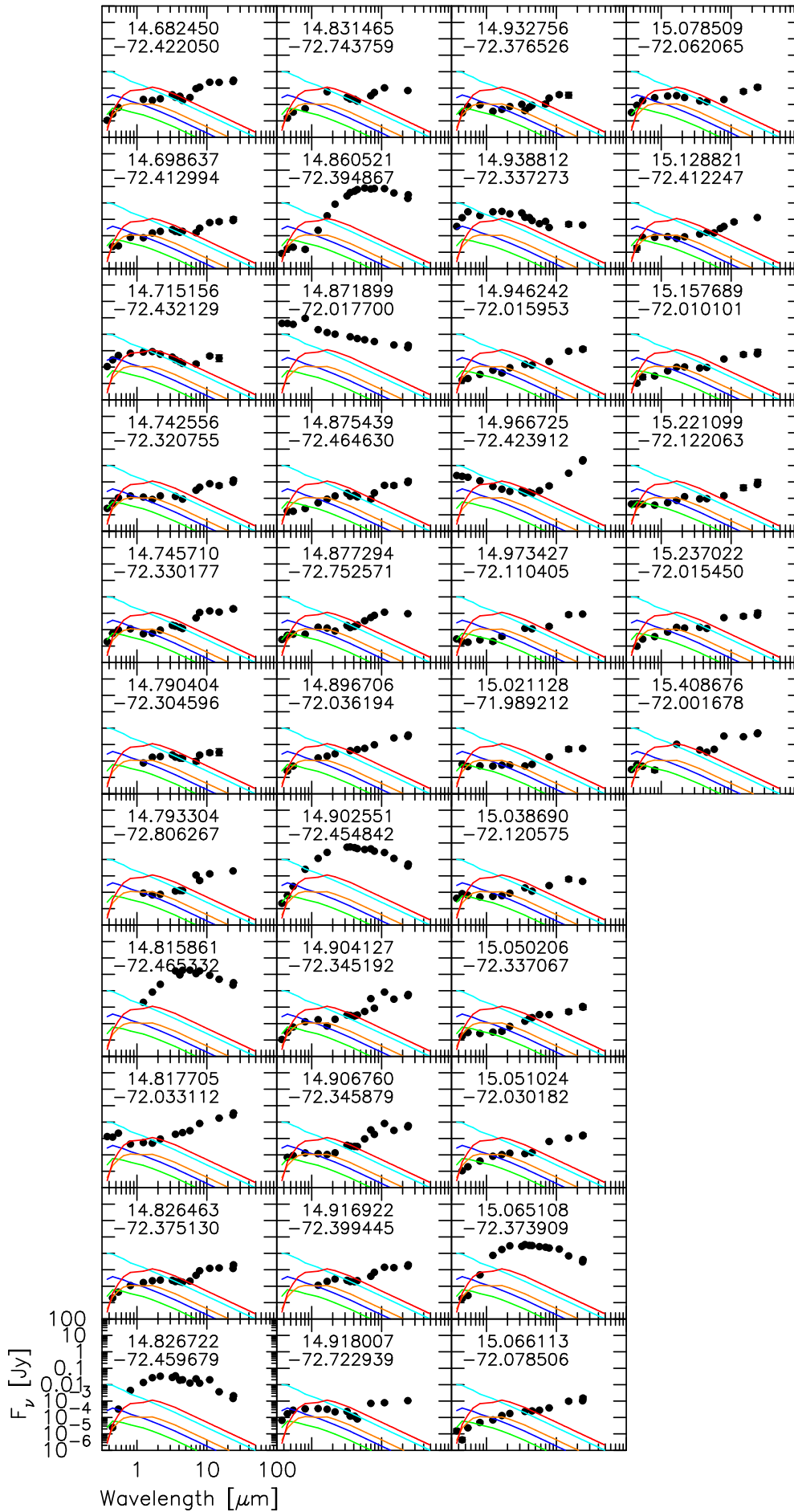


Fig. 7. The spectral energy distributions of very red AKARI/IRC sources. Note that the vertical axis is in flux densities

marized in Table 4. Judging from the query results and shapes of the SEDs, there are mainly four types of objects in the sample: (1) dusty AGB stars; (2) emission line stars or early-type stars; (3) candidates of young stellar objects (YSOs) or post-AGB stars or planetary nebulae (PNe); (4) X-ray sources. One thing to note is that the star SMC13.876909–72.839333 is classified as candidate YSO in SIMBAD, but this star is likely to be a planetary nebula (George Jacoby, private communication; Stanghellini et al. 2003)

#### 4.4.1. Dusty AGB stars

Recently, Gruendl et al. (2008) discovered extremely red carbon-rich AGB stars in the LMC, whose SED attains its maximum at around or beyond  $10\ \mu\text{m}$ . According to Gruendl et al. (2008), the mass loss rates of such extremely red sources are as high as a few times  $10^{-4}\ M_{\odot}/\text{yr}$ , much higher than expected from their luminosities of about  $7000 - 8000\ L_{\odot}$ . In this context, similar red objects are detected in the SMC, such as SMC12.428394–73.038963, SMC12.457850–72.754089, SMC13.791426–73.712502, SMC13.878624–73.631279, SMC13.952203–72.791412, SMC14.170046–72.907120, SMC14.278221–72.827110, and SMC14.860521–72.394867, in addition to known ones listed in Table 4. These stars are new candidates of dusty AGB stars in the SMC, where the mean metallicity is about a half of that of that of the LMC. These sources may be important to understand how mass loss depends on the metallicities (Matsuura et al. 2005; Sloan et al. 2008) and ultimately to understand the stellar evolution of intermediate-mass stars. Their mass-loss rates, and pulsation properties will be discussed in future, using AKARI’s infrared spectroscopic data and IRSF/SIRIUS near-infrared monitoring survey data.

#### 4.4.2. Early-type stars with infrared excesses

Bolatto et al. (2006) detected about 190 early-type (i.e., MK spectral class of O, B, and A) stars with  $24\ \mu\text{m}$  excess in the SMC. Our observation confirmed the existence of early-type stars with infrared excess in the SMC (see, for example, SMC12.639604–72.795998). It is clear that AKARI’s S7, S11 and L15 data reinforce the presence of infrared excesses among early-type stars in the SMC. The thermal bremsstrahlung (free-free) emission, and/or the presence of cold dust (with a characteristic temperature of about 150 K) may explain the amount of infrared excess for some stars (e.g., SMC12.408465–73.102928).

#### 4.4.3. Post-AGB stars or YSO candidates

Post-AGB stars are in their short transition phase between the end of AGB and (proto-)planetary nebula. Due to the short life time ( $10^2 - 10^4\ \text{yr}$ ; e.g., Vassiliadis & Wood 1994) and difficulty in distinguishing them from young YSOs, only three Post-AGB stars have been identified to date in the SMC (IRAS00350–7436; Whitelock et al. 1989, KVS2000 MIR1; Kučinskas et al. 2000, MSX SMC 029; Kraemer et al. 2006). In the Galactic cases, post-AGB stars are in general luminous ( $10^3 - 10^4\ L_{\odot}$ ) and they usually have double-peak SEDs, with the optical peak of hot (MK spectral types earlier than G) central stars and the infrared peak of circumstellar dust (e.g., Szczerba et al. 2007). Figure 7 indicates that some of the sources are

likely to have double-peaked SEDs. We calculated bolometric luminosities for all the 204 sources by using a cubic spline to interpolate the spectral energy distributions and integrate them from the shortest wavelength at which the flux is available to  $24\ \mu\text{m}$ . We assumed a distance modulus of 18.95 mag to the SMC. For most of the sources, the calculated luminosities may be underestimated to a large extent because the fluxes longward of  $24\ \mu\text{m}$  are not included. Therefore the luminosities calculated should be only lower limits. Also, we have to note that the luminosities are rather uncertain, because they are sensitive to the changes of the value of the interstellar extinctions and color correction, and also to light variations if any. There are twelve sources with double-peak like SED and calculated luminosity brighter than  $1000\ L_{\odot}$ . These twelve sources are tabulated in Table 5.

**Table 5.** Sources with double-peak like SED and calculated luminosity brighter than  $1000\ L_{\odot}$ .

Name	Luminosity [ $L_{\odot}$ ]
SMC12.371058–73.449753	1086
SMC12.697147–72.803398	1807
SMC12.821114–72.425980	2065
SMC12.829427–72.676781	2156
SMC12.885851–72.713806	2403
SMC13.453571–73.325600	1094
SMC13.479052–73.317139	2951
SMC13.514072–73.327576	13592
SMC13.835342–73.360657	2764
SMC14.026985–72.789665	2147
SMC14.574934–72.746552	1126
SMC14.966725–72.423912	2127

Six among the twelve sources have identifications in the SIMBAD databases (see Table 4). One is classified as YSO candidates, and four are classified as emission line stars, and one is classified as a Cepheid variable. Follow-up spectroscopic observations would be needed for their full characterization.

## 5. Summary

We carried out imaging and spectroscopic observations for patchy areas in the SMC using IRC onboard AKARI. In this paper we outlined the survey, and presented bright point source lists. The point source lists are cross-identified with the existing ground-based optical and near-infrared photometric survey catalogs, and also with the *Spitzer* SAGE-SMC catalog. The spectral energy distributions of a wide variety of sources are inspected, resulting in finding new candidates of dusty red giants and post-AGB stars. We also confirmed the existence of early-type stars with strong infrared excesses, which are found by Bolatto et al. (2006).

## Acknowledgements

Y.I. thanks Dr. George Jacoby for providing him with the Planetary Nebulae catalog in the SMC before publication. AKARI is a JAXA project with the participation of ESA. This work is supported by the Grant-in-Aid for Encouragement of Young Scientists (B) No. 21740142 from the Ministry of Education, Culture, Sports, Science and Technology of Japan. This research has made use of the SIMBAD database, operated at CDS, Strasbourg, France. This publication makes use of data products from the Two Micron All Sky Survey, which is a joint project of the University of Massachusetts and the Infrared Processing and Analysis Center/California Institute of Technology, funded by the National Aeronautics and Space Administration and the National Science Foundation. This research has made use of the NASA/IPAC Infrared Science Archive, which is operated by the Jet Propulsion Laboratory, California Institute of Technology, under contract with the National Aeronautics and Space Administration. The Digitized Sky Surveys were produced at the Space Telescope Science Institute under U.S. Government grant NAG W-2166. The images of these surveys are based on photographic data obtained using the Oschin Schmidt Telescope on Palomar Mountain and the UK Schmidt Telescope.

## References

- Benjamin R.A., Churchwell E., Babler B.L., et al., 2003, *PASP*, 115, 953
- Bolatto A.D., Simon J.D., Stanimirović S., et al., 2006, *ApJ*, 655, 212
- Cardelli J.A., Clayton G.C., & Mathis J.S., 1989, *ApJ*, 345, 245
- Cioni M.R., Loup C., Habing H.J., et al., 2000, *A&AS*, 144, 235
- Cox A.N., 2000, *Allen's Astrophysical Quantities*, 4th edition, Springer-Verlag, New York
- Dickey J.M., Mebold U., Stanimirovic S., et al., 2000, *ApJ*, 536, 756
- Dufour R. F., Shields G. A., & Talbot R. J., 1982, *ApJ*, 252, 461
- Dufour R. F., 1984, *IAUS*, 108, 353, in *Structure and evolution of the Magellanic Clouds; Proceedings of the Symposium, Tuebingen, West Germany, September 5-8, 1983 (A85-26576 11-90)*. Dordrecht, D. Reidel Publishing Co., 1984, p. 353-360
- Egan M.P., Price S.D., Kraemer K.E., et al., 2003, in *Air Force Research Laboratory Technical Report*, Vol. AFRL-VS-TR-2003-1589
- Fazio G.G., Hora J.L., Allen L.E., et al., 2004a, *ApJS*, 154, 10
- Gordon K.D., Clayton G.C., Misselt K.A., et al., 2003, *ApJ*, 594, 279
- Gordon K.D., et al., 2010, in preparation
- Gruendl R.A., Chu Y.-H., Seale J.P., et al., 2008, *ApJ*, 688, 9
- Israel F.P., & Schwering P.B., et al., 1986, *ASSL*, 124, 383
- Ita Y., Tanabé T., Matsunaga N., et al., 2002, *MNRAS*, 337, 31
- Ita Y., Tanabé T., Matsunaga N., et al., 2004a, *MNRAS*, 347, 720
- Ita Y., Tanabé T., Matsunaga N., et al., 2007, *PASJ*, 59, 437
- Ita Y., Onaka T., Kato D., et al., 2008, *PASJ*, 60, 435
- Kato D., Nagashima C., Nagayama T., et al., 2007, *PASJ*, 59, 615
- Kraemer K.E., Sloan G.C., Bernard-Salas J. et al, 2006, *ApJ*, 652, 25
- Kučinskas A., Vanevičius V., Sauvage M., et al., 2000, *A&A*, 353, 21
- Kučinskas A., Dobrovolskas V., Lazauskaitė R., 2008, *Baltic Astronomy* 17, 283
- Lorente R., Onaka T., Ita Y., et al., 2007, *AKARI IRC Data User's Manual ver. 1.3*, <http://www.ir.isas.jaxa.jp/AKARI/Observation/>
- Matsuura M., Zijlstra A.A., van Loon J.Th., et al., 2005, *A&A*, 434, 691
- Meixner M., Gordon K.D., Indebetouw R., et al., 2006, *AJ*, 132, 2288
- MIPS Data Handbook, version 3.3, 2007 August 07, <http://ssc.spitzer.caltech.edu/mips/dh/mipsdatahandbook3.3.pdf>
- Murakami H., Baba H., Barthel P., et al., 2007, *PASJ*, 59, S369
- Nikolaev S., & Weinberg M.D., 2000, *ApJ*, 542, 804
- Ohyama Y., Onaka T., Matsuhara H., et al., 2007, *PASJ*, 59, S411
- Onaka T., Matsuhara H., Wada T., et al., 2007, *PASJ*, 59, S401
- Rebeiro E., Azzopardi M., & Westerlund B.E., 1993, *A&AS*, 97, 63
- Rieke G.H., Young E.T., Engelbracht C.W., et al., 2004, *ApJS*, 154, 25
- Skrutskie M.F., Cutri R.M., Stiening R., et al., 2006, *AJ*, 131, 1163
- Sloan G.C., Kraemer K.E., Wood P.R., et al., 2008, *ApJ*, 686, 1056
- Stanghellini L., Shaw R.A., Balick B., et al., 2003, *ApJ*, 596, 997
- Stanimirovic S., Staveley-Smith L., van der Hulst J.M., et al., 2000, *MNRAS*, 315, 791
- Subramanian A., & Subramanian S., 2008, *Proc. IAU Symp. No 256, The Magellanic System: Stars, Gas and Galaxies*, eds. Jacco Th. van Loon & Joana M. Oliveira (astro-ph:0809.2637)
- Szczerba R., Siódmiak N., Stasińska G., et al., 2007, *A&A*, 469, 799
- Tanabé T., et al., 2008, *PASJ*, submitted
- Westerlund B.E., 1997, *The Magellanic Clouds*. Cambridge Univ. Press, Cambridge
- Whitlock P.A., Feast M.W., Menzies J.W. et al., 1989, *MNRAS*, 238, 769
- Udalski A., Soszyński M., Szymański M., 1999, *AcA*, 49, 437
- Vassiliadis E. & Wood P.R., 1994, *ApJS*, 92, 125
- Zaritsky D., Harris J., Thompson I.B., et al., 2002, *AJ*, 123, 855

**Table 4.** SIMBAD query results for 204 red sources selected in section 4.4. Seventy-one sources have identified by the SIMBAD database using a 3" search radius.

Name	Main object type <sup>1</sup>
SMC12.123491–73.085312	Candidate YSO
SMC12.265644–73.088905	Carbon star
SMC12.285033–73.040665	High proper-motion star
SMC12.357609–73.201149	AGB star
SMC12.362229–73.500290	Carbon star
SMC12.371058–73.449753	Candidate YSO
SMC12.381301–73.121201	Carbon star
SMC12.408465–73.102928	Emission line star
SMC12.428394–73.038963	Variable star
SMC12.503441–72.690338	Carbon star
SMC12.530446–73.523582	AGB star
SMC12.539059–73.214767	Carbon star
SMC12.555729–73.186707	Carbon star
SMC12.585061–73.187820	High Mass X-ray Binary
SMC12.616507–72.691696	Carbon star
SMC12.639604–72.795998	Star
SMC12.649479–72.781296	Candidate YSO
SMC12.650483–72.769417	Emission line star
SMC12.654076–73.148079	Variable star
SMC12.680836–72.782333	Candidate YSO
SMC12.693326–73.135406	Emission line star
SMC12.693772–72.778503	Emission line star
SMC12.697147–72.803398	Cepheid variable
SMC12.703513–73.101646	Carbon star
SMC12.742255–73.132561	Emission line star
SMC12.747120–72.732399	Emission line star
SMC12.752715–72.422050	Carbon star
SMC12.783894–73.228401	Carbon star
SMC12.806942–73.176620	Carbon star
SMC12.814873–73.160889	Eclipsing binary
SMC12.829427–72.676781	Emission line star
SMC12.862647–72.436852	Planetary Nebula
SMC13.004549–72.402351	Star
SMC13.410227–73.295364	Variable star
SMC13.412084–73.555298	Carbon star
SMC13.427867–73.618950	Planetary Nebula
SMC13.489193–73.575768	Carbon star
SMC13.568759–73.273514	Candidate YSO
SMC13.695276–73.227066	Carbon star
SMC13.835342–73.360657	Emission line star
SMC13.876909–72.839333	Candidate YSO / Planetary nebula
SMC13.888869–73.305130	X-ray source
SMC13.952203–72.791412	Variable star
SMC13.971072–72.874924	Candidate YSO
SMC13.977923–73.193428	Carbon star
SMC13.998604–72.879395	Quasar
SMC14.026985–72.789665	Emission line star
SMC14.027878–72.795395	Candidate YSO
SMC14.051175–72.775162	Candidate YSO
SMC14.085259–72.753120	Candidate YSO
SMC14.101144–72.875122	Candidate YSO
SMC14.123505–72.855370	Carbon star
SMC14.201462–72.805565	Emission line star
SMC14.278221–72.827110	Variable star
SMC14.316910–72.801575	Carbon star

**Table 4.** (Continued.)

Name	Main object type <sup>1</sup>
SMC14.488285–72.654518	Candidate YSO
SMC14.521901–72.652542	Candidate YSO
SMC14.536167–72.652878	Candidate YSO
SMC14.678715–72.454956	Planetary Nebula
SMC14.815861–72.465332	Carbon star
SMC14.817705–72.033112	Planetary Nebula
SMC14.826722–72.459679	Carbon star
SMC14.871899–72.017700	Emission line object
SMC14.896706–72.036194	X-ray source
SMC14.902551–72.454842	Carbon star
SMC14.906760–72.345879	Candidate YSO
SMC14.946242–72.015953	X-ray source
SMC14.966725–72.423912	Emission line star
SMC15.021128–71.989212	X-ray source
SMC15.050206–72.337067	X-ray source
SMC15.065108–72.373909	Carbon star

<sup>1</sup> refer <http://simbad.u-strasbg.fr/simbad/sim-display?data=otypes> for the details of object classification in SIMBAD.